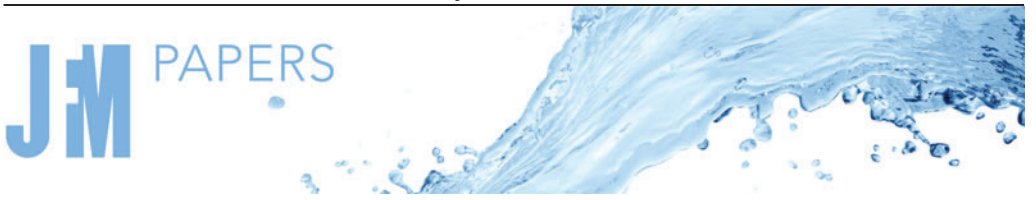
CrossMark

J. Fluid Mech. (2022), *vol*. 949, A51, doi:10.1017/jfm.2022.814



The influence of temporal heating modulation on non-isothermal floating droplet dynamics

Alexander Nepomnyashchy[1] **and Ilya Simanovskii**[1]

[1]Department of Mathematics, Technion – Israel Institute of Technology, 32000 Haifa, Israel

(Received 24 March 2022; revised 9 July 2022; accepted 12 September 2022)

The action of temporal heating modulation on Marangoni flows in a droplet on a liquid substrate is investigated. The problem is studied numerically in the framework of long-wave amplitude equations and precursor model. It is shown that temporal modulation can lead to a change of the droplet shape. Specifically, rhombic droplets have been obtained. A modulated cooling from below can lead to periodic or quasiperiodic oscillations or the droplet's decomposition.

Key words: nonlinear instability

1. Introduction

It is known that the conductive state of a thin liquid film heated from below is subject to two kinds of monotonic Marangoni instability, the short-wave cellular instability (Pearson 1958) and the long-wave deformational instability (Sternling & Scriven 1964; Smith 1966). The latter type of instability dominates in very thin films or under microgravity conditions.

The manifestations of the Marangoni instabilities in multilayer fluid systems are much more diverse (for a review, see Nepomnyashchy, Simanovskii & Legros (2012)). The instabilities can develop for heating both from below and from above, and it can be both monotonic and oscillatory (Nepomnyashchy & Simanovskii 2007).

A specific kind of a multilayer fluid system is a droplet on a liquid substrate ('liquid lens'). The processes in that system have important applications in engineering, including liquid-phase microextraction (Yamini, Rezazadeh & Seidi 2019), droplet-based microfluidics (Labanieh *et al.* 2015), oil-spill cleanup (Ju *et al.* 2019), droplet-based floating electrodes (Chen *et al.* 2018) and DNA studies (Shimazaki *et al.* 2021). In some experiments, oscillatory convection flows in a droplet generated by the thermocapillary effect and buoyancy were observed (Rybalko, Magome & Yoshikawa 2004; Song *et al.* 2014; Buffone 2019). Recently, instabilities of the flow in a floating droplet, similar to

† Email address for correspondence: yuri11@inter.net.il

© The Author(s), 2022. Published by Cambridge University Press

https://doi.org/10.1017/jfm.2022.814 Published online by Cambridge University Press

those formerly found in a two-layer film, have been revealed by numerical simulations in Nepomnyashchy & Simanovskii (2021).

In applications, it can be important to control the instability, i.e. to eliminate it or support a definite kind of the flow. The most widespread tool for excitation and suppression of instabilities is vibration (Gershuni & Lyubimov 1998). In the case of Marangoni instability caused by heating, the temporal modulation of heating intensity can be a more efficient way for instability excitation and control (Gershuni, Nepomnyashchy & Velarde 1992; Or & Kelly 2002; Smorodin *et al.* 2009). Specifically, in the case of an oscillatory Marangoni instability, the modulation of the substrate temperature can lead to the parametric excitation of Marangoni waves (Nepomnyashchy & Simanovskii 2015). In the supercritical parameter region, the action of heating modulation on the nonlinear Marangoni wave either creates a two-frequency quasiperiodic motion or leads to frequency locking (Nepomnyashchy & Simanovskii 2020). The influence of a temporal parameter modulation on the droplet instabilities has not yet been studied.

The direct solution of equations governing droplet dynamics is rather difficult, because in addition to the calculation of flow fields, it is necessary to track interfaces and compute the motion of the triple line. For that goal, one applies numerical methods, e.g. the boundary integral method (Manga & Stone 1995), the volume of fluid method (Scardovelli & Zaleski 1999) and the level set method (Smith, Ottino & de la Cruz 2004). A significant simplification of the mathematical model can be achieved in the case of a slender droplet by means of the long-wave approximation (Oron, Davis & Bankoff 1997). Still, the description of the triple-line motion is technically difficult due to numerous boundary and matching conditions (Kriegsmann & Miksis 2003; Huth *et al.* 2015). Those difficulties can be avoided by means of the precursor model similar to that developed in the case of a droplet on a solid surface (Craster & Matar 2006).

In the present paper, the dynamics of a droplet on a liquid substrate under the action of a temporal cooling modulation on the bottom is investigated. The long-wave approximation and precursor model are applied. We show that the temporal modulation can significantly change the shape of the droplet and lead to the appearance of rhombic droplets.

The structure of the paper is as follows. The formulation of the problem is given in § 2. In § 3, the numerical approach as well as droplet oscillations under the action of temporally modulated heating are described. Section 4 contains concluding remarks.

2. Formulation of the problem

We consider a droplet of liquid 2 that floats on a layer of liquid 1, and it is in contact with the gas phase 3 (see figure 1). The gravity acceleration is g. The mth fluid has density ρ_m, dynamic viscosity η_m and thermal conductivity κ_m. The deformable interfaces are described by equations $z = H_1(x, y, t)$ and $z = H_2(x, y, t)$.

In order to avoid technical difficulties with the description of the triple-line dynamics, we apply the precursor model that presents the droplet and the liquid substrate as a two-layer film.

Following Craster & Matar (2006), we assume that outside the droplet, liquid 1 is separated from the gas phase by an ultrathin precursor film of liquid 2. The balance between forces on the triple line is achieved by an appropriate choice of the disjoining pressure. Far from the droplet, the equilibrium thickness of layer 1 is H_1^0, and the thickness of the precursor film is $H_2 - H_1 = H_\infty$ (see figure 1).

Let us emphasize that the precursor model can be applied in different cases. If the spreading coefficient $S = \sigma_{31} - \sigma_{12} - \sigma_{23} < 0$ (partial wetting), using an artificial precursor is just a computational approach. When $S > 0$ but the Hamaker constant A_2,

https://doi.org/10.1017/jfm.2022.814 Published online by Cambridge University Press

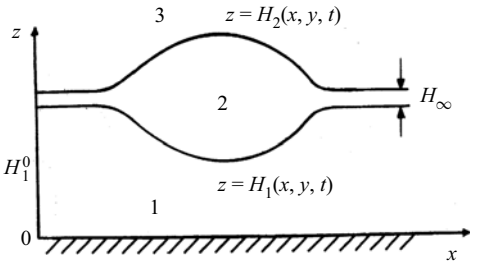


Figure 1. Geometric configuration of the region and coordinate axes.

which characterizes the interaction of fluids 1 and 3 through the film of fluid 2, is positive, an ultrathin film of fluid 2 is created rather than a macroscopic layer of fluid 2 (pseudopartial wetting). From the macroscopic point of view, both cases are identical.

We do not consider the flow and the heat transfer in the gas. The viscous stresses at the upper boundary are neglected. It is assumed that the temperature of the gas phase is T_g, and the heat exchange coefficient at the liquid–gas interface is q. The temperature of the solid substrate is $T_s(x, y, t)$. The case $T_s > T_g$ ($T_s < T_g$) corresponds to heating (cooling) the system from the side of the substrate. Below we consider the case of cooling, where the liquid substrate itself is stable, and the instability is caused by the presence of the liquid lens.

Assuming that the temperature differences in the system are not too large, we disregard the dependence of liquid parameters on the temperature, with the following exception. Because the Marangoni convection is caused by the dependence of the interfacial tension coefficients on the temperature, that dependence has to be taken into account. The interfacial tension coefficients on the lower and upper surfaces of the droplets, $\sigma_1 \equiv \sigma_{12}$ and $\sigma_2 \equiv \sigma_{23}$, are linear functions of temperature T: $\sigma_1 = \sigma_1^0 - \alpha_1 T$ and $\sigma_2 = \sigma_2^0 - \alpha_2 T$, where α_1 and α_2 are constants.

Later on, we consider a slender droplet, i.e. the slopes of both droplet interfaces are small. Thus, the droplet looks as a thin film of liquid 2 with variable thickness sandwiched between fluids 1 and 3. Therefore, one may expect that the droplet can be subject to long wave instabilities similar to those found in the case of layers. In the present paper, we concentrate on the analysis of that kind of instabilities. In this case, we can apply the mathematical model governing the long-wave dynamics of non-isothermal liquid layers that has been derived using the lubrication approximation in Pototsky *et al.* (2005) (see also Nepomnyashchy & Simanovskii 2007, 2010, 2012). Let us note that this approach does not allow us to reveal short-wave instabilities (e.g. a fingering instability of the triple line) characterized by a horizontal scale different from that determined by the droplet size, if any.

In the framework of the long-wave approach, shapes of interfaces $z = H_1$ and $z = H_2$ depend on the scaled horizontal coordinates $X = \epsilon x$ and $Y = \epsilon y$, $\epsilon \ll 1$, rather than on x and y. Also, it is assumed that they depend on the scaled time variable $\tau = \epsilon^2 t$. A comprehensive description of the long-wave approach can be found in Oron *et al.* (1997).

The problem is presented in the non-dimensional form using the equilibrium thickness of the lower layer, H_1^0, as the vertical length scale. The choice of the horizontal scale L^* is arbitrary (Nepomnyashchy & Simanovskii 2012). We choose

$$\tau^* = \frac{\eta_1 (L^*)^4}{\sigma_1^0 (H_1^0)^3} \tag{2.1}$$

https://doi.org/10.1017/jfm.2022.814 Published online by Cambridge University Press

as a time scale and

$$p^* = \frac{\sigma_1^0 H_1^0}{(L^*)^2} \tag{2.2}$$

as a pressure scale.

The non-dimensional parameters of the problem are defined as follows:

$$M(t) = \frac{\alpha_1 (T_s(t) - T_g)}{\sigma_1^0} \left(\frac{L^*}{H_1^0} \right)^2 \tag{2.3}$$

is the modified Marangoni number, which is a function of the horizontal coordinates,

$$Bi = \frac{q H_1^0}{\kappa_2} \tag{2.4}$$

is the Biot number, $\eta = \eta_1/\eta_2$, $\kappa = \kappa_1/\kappa_2$, $\sigma = \sigma_2^0/\sigma_1^0$, $\alpha = \alpha_2/\alpha_1$, $\rho = \rho_2/\rho_1$ and

$$Bo = \frac{g\rho_1 (L^*)^2}{\sigma_1^0} \tag{2.5}$$

is the Bond number.

In the framework of the lubrication approximation, the velocity and pressure fields are enslaved to the deformations of interfaces. The temporal evolution of those deformations is governed by the volume conservation equations:

$$h_{1\tau} + \nabla \cdot \boldsymbol{q}_1 = 0, \quad h_{2\tau} + \nabla \cdot \boldsymbol{q}_2 = 0, \tag{2.6a,b}$$

$$\boldsymbol{q}_1 = f_{11} \nabla p_1 + f_{12} \nabla p_2 + \boldsymbol{q}_1^{\mathrm{T}}, \quad \boldsymbol{q}_2 = f_{21} \nabla p_1 + f_{22} \nabla p_2 + \boldsymbol{q}_2^{\mathrm{T}}. \tag{2.7a,b}$$

All the quantities in (2.6a,b), (2.7a,b) are non-dimensional; $h_j = H_j/H_1^0$, $p_j = P_j/p^*$, $j = 1, 2$.

The expressions for mobilities f_{ij}, $i, j = 1, 2$, are

$$f_{11} = -\frac{1}{3} h_1^3, \quad f_{12} = -\frac{1}{2} h_1^2 (h_2 - h_1), \tag{2.8a,b}$$

$$f_{21} = \frac{1}{6} h_1^3 - \frac{1}{2} h_1^2 h_2, \quad f_{22} = (h_2 - h_1) \left[h_1^2 \left(\frac{1}{2} - \frac{\eta}{3} \right) + h_1 h_2 \left(-1 + \frac{2\eta}{3} \right) - \frac{\eta}{3} h_2^2 \right]. \tag{2.9a,b}$$

The expressions for pressures,

$$p_1 = -\nabla^2 h_1 - \sigma \nabla^2 h_2 + Boh_1 + Bo\rho (h_2 - h_1) + w_1(h_1, h_2), \tag{2.10}$$

$$p_2 = -\sigma \nabla^2 h_2 + Bo\rho h_2 + w_2(h_1, h_2), \tag{2.11}$$

include the contributions of the Laplacian pressures, hydrostatic pressures and disjoining pressures.

Fisher & Golovin (2005) have suggested the following expressions for the disjoining pressures in a two-layer film:

$$w_1 = \frac{a_0 - a_1 - a_2}{h_2^3} + \frac{a_1}{h_1^3}, \quad w_2 = \frac{a_0 - a_1 - a_2}{h_2^3} + \frac{a_2}{(h_2 - h_1)^3}, \tag{2.12a,b}$$

where a_0, a_1 and a_2 are non-dimensional Hamaker constants. Because the thickness of liquid layer 1 is always macroscopic, we can take $w_1 = 0$. In layer 2, we apply the following

https://doi.org/10.1017/jfm.2022.814 Published online by Cambridge University Press

expression for the disjoining pressure:

$$w_2 = \frac{a}{(h_2 - h_1)^3}\left[1 - \left(\frac{h_\infty}{h_2 - h_1}\right)^3\right], \tag{2.13}$$

where a is the non-dimensional Hamaker constant, which is related to the dimensional Hamaker constant A as

$$a = \frac{A(L^*)^2}{6\pi\sigma_1^0(H_1^0)^4}, \tag{2.14}$$

and $h_\infty = H_\infty/H_1^0$ (for details, see Craster & Matar (2006) and Pototsky, Oron & Bestehorn (2019)).

The non-dimensional expressions for the rates of the thermocapillary flows are

$$\boldsymbol{q}_1^{\mathrm{T}} = -\frac{h_1^2}{2}\nabla\{M[1 + d(\alpha\kappa - Bih_1\}, \tag{2.15}$$

$$\boldsymbol{q}_2^{\mathrm{T}} = -\frac{\eta\alpha\kappa}{2}h_2^2\nabla(Md) + \frac{(2h_2 - h_1)h_1}{2}\nabla\{M[-1 + Bih_1d - \alpha\kappa(1 - \eta)d]\}, \tag{2.16}$$

where

$$d = [\kappa + Bi(1 - \kappa)h_1 + Bi\kappa h_2]^{-1}. \tag{2.17}$$

3. Nonlinear simulations

3.1. *Numerical approach*

In the present section, we describe the results of numerical simulations performed in the framework of system (2.6*a*,*b*)–(2.16). The evolution equations were discretized by central differences for spatial derivatives and solved using an explicit scheme. In the framework of this scheme, the fields on the next time step have been calculated through the corresponding fields on the previous time step. The convergence of that approach with the decrease of the mesh size was formerly studied by Nepomnyashchy & Simanovskii (2015). Periodic boundary conditions have been applied on the boundaries of the computational region $L \times L$, $L = 240$. Periodic boundary conditions correspond to an infinite system of droplets moving synchronously.

Recall that in the present paper we assume that the characteristic horizontal scale of the surface deformations is significantly larger than the thicknesses of the droplet and the substrate layer. The computations have been performed in the computational region, using a grid of 80×80.

Actually, the fields h_1 and h_2 are rather smooth; thus the 80×80 grid gives a good resolution of large-scale wave patterns. The choice of parameters in the present paper has been done after some trial simulations on 100×100 and 120×120 grids.

Some additional convergence tests on 60×60, 80×80 and 100×100 grids can be found in figure 4 of Nepomnyashchy & Simanovskii (2015), and no qualitative changes have been observed.

The simulations have been carried out during at least 10^6 non-dimensional time units. In all the simulations, the change of the fields h_m, $m = 1, 2$, was less than 0.3 %. The time step typically changed between 0.00125 and 0.005, which is significantly below the linear

https://doi.org/10.1017/jfm.2022.814 Published online by Cambridge University Press

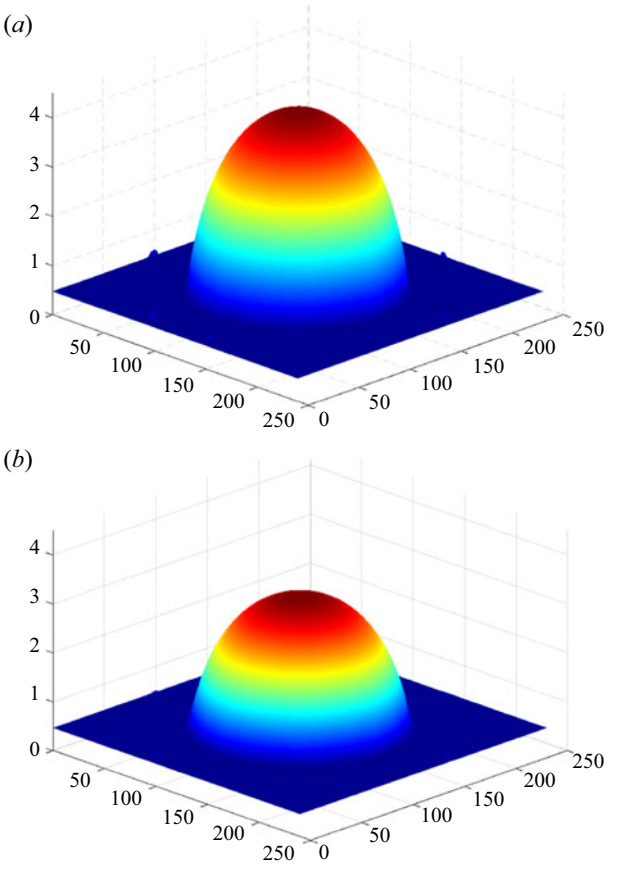


Figure 2. The stationary shapes of (*a*) interface $h_2(X, Y)$ and (*b*) interface $h_1(X, Y)$ for $M = -2$, $Bo = 0$, $Bi = 20$, $\tau = 10^6$.

scheme stability boundary. No quantitative changes have been observed for simulations made with different time steps.

We used two kinds of initial conditions. First, we applied the initial conditions

$$h_1(X, Y, 0) = 1; \quad h_2(X, Y, 0) = h_- + h_+ \exp\{-[(X - L/2)^2 + (Y - L/2)^2]/R^2\}, \tag{3.1a,b}$$

i.e. a droplet of liquid 2 with a Gaussian shape was imposed on a flat layer of liquid 1. In some other simulations, we used the shape of the droplet obtained in the previous simulations carried out for a different set of parameters as the initial condition, and continued simulations for the new set of parameters.

The system under consideration is characterized by five non-dimensional parameters that correspond to the ratios of physical parameters and three other parameters that describe the external actions on the system (non-dimensional temperature difference, heat transfer on the liquid–gas interface and gravity). It looks impossible to analyse the influence of all those parameters. Therefore, we restrict ourselves to the investigation of a particular system of liquids, as is usually done in the case of multilayer systems.

In the present paper, we perform computations for the system of fluorinert FC70 (liquid 1) and silicone oil 10 (liquid 2). This system of liquids was used in microgravity experiments (see, e.g. Géoris *et al.* 1999). We applied the following set of liquid parameters

https://doi.org/10.1017/jfm.2022.814 Published online by Cambridge University Press

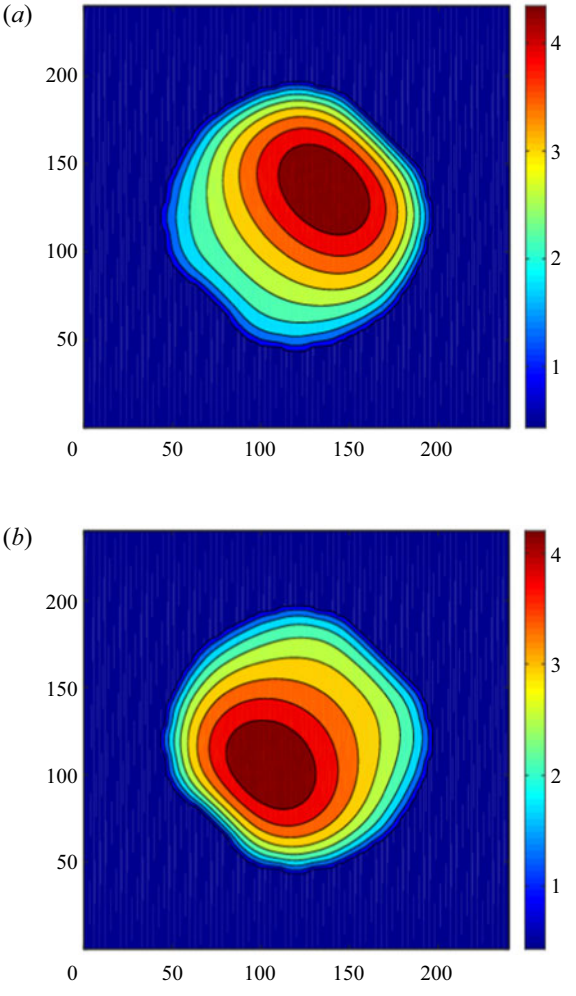


Figure 3. A snapshot of the fields of $h_2(X, Y, \tau)$ at (*a*) $\tau = 7 \times 10^5$ and (*b*) $\tau = 7.15 \times 10^5$ for $M = -2.5$, $Bo = 0$, $Bi = 20$.

that was formerly used in simulations of Marangoni instability in two-layer systems (Nepomnyashchy & Simanovskii 2012): $\eta = 3.04, \kappa = 0.522, \alpha = 2, \rho = 0.482, \sigma = 2.6$. $h_- = 1.02$, $h_+ = 1$, $R = 60$, $h_\infty = 0.01$, $Bo = 0$ and $Bi = 20$. The value of a_2 is chosen equal to 3×10^{-6} (see Nepomnyashchy & Simanovskii 2021).

Note that in the absence of gravity, a liquid layer with a deformable interface is subject to a monotonic Marangoni instability for arbitrary small $M > 0$, i.e. for arbitrary weak heating from below (Sternling & Scriven 1964). That instability is not saturable, and it leads to the rupture of the substrate layer. The temperature disturbance caused by the droplet acts as a 'seed' of instability. Therefore, in the presence of the temperature gradient, one can expect the existence of a stable configuration containing a droplet on a layer flat on the infinity only if $M < 0$, i.e. by cooling from below.

https://doi.org/10.1017/jfm.2022.814 Published online by Cambridge University Press

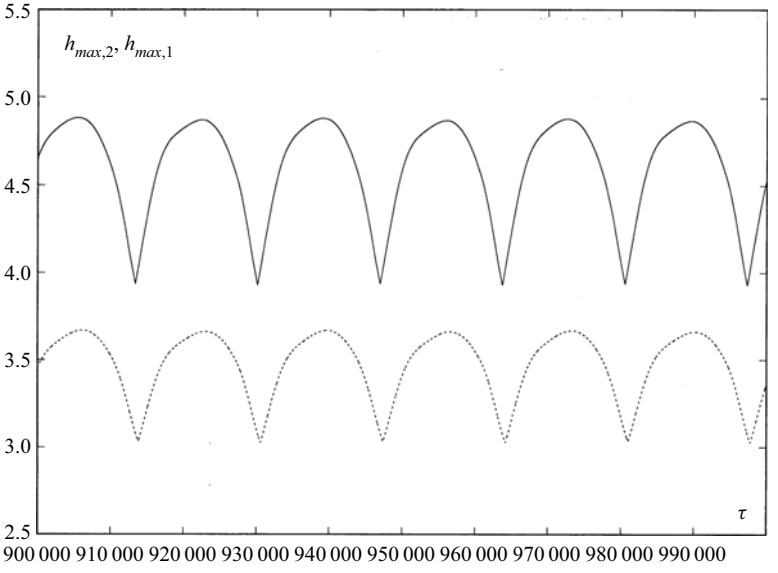


Figure 4. The oscillations of $h_{max,2}(\tau)$ (solid line) and $h_{max,1}(\tau)$ (dashed line) for $M = -2.5$, $Bo = 0$, $Bi = 20$.

3.2. *Nonlinear regimes in the absence of modulation*

In the present subsection, we describe briefly some results of numerical simulations carried out for $M = \text{const.}$ (for details, see Nepomnyashchy & Simanovskii (2021)).

It is known that in the absence of gravity and the thermocapillary effect ($M = Bo = 0$), both interfaces of an equilibrium droplet are spherical caps. The exact formulas that follow from the balance of interfacial tensions on the triple line are given, for example, by Princen (1969). In the long-wave limit, these interfaces become paraboloids:

$$h_1 = 1 + a(r^2 - r_0^2), \quad h_2 = 1 - \frac{a}{\sigma}(r^2 - r_0^2); \quad r < r_0, \tag{3.2a,b}$$

where r is the radial coordinate, a is a constant and r_0 is the droplet's radius. The paraboloidal surface profiles satisfy (2.6*a*,*b*)–(2.11). They correspond to constant pressures in the droplet and in the substrate and to zero flow rates.

For moderate values of $|M|$ the droplet is stationary and axisymmetric. The isolines $h_1(X, Y)$ and $h_2(X, Y)$ are perfectly circular. However, the shapes of the interfaces change drastically. While in the case $M = 0$ the second derivatives $\mathrm{d}^2h_1/\mathrm{d}r^2$ and $\mathrm{d}^2h_2/\mathrm{d}r^2$ are of different signs, at $M < 0$ they are typically of the same sign, at least for sufficiently large $Bi|M|$. Indeed, in the latter case the terms $\boldsymbol{q}_1^{\mathrm{T}}$ and $\boldsymbol{q}_2^{\mathrm{T}}$ prevail in expression (2.7*a*,*b*). At large $Bi|M|$, the leading-order terms in expressions (2.15) and (2.16) are proportional to

$$Bih_1 d \sim \frac{h_1}{(1-\kappa)h_1 + \kappa h_2}. \tag{3.3}$$

Therefore, the flow rates vanish when $h_1/h_2 = \text{const.}$ In other words, the lower surface of the droplet $z = h_1(r)$ is adjusted to its upper surface $z = h_2(r)$ in such a way that the temperature at the interface between the droplet and the substrate is nearly constant, so that the thermocapillary stress that creates thermocapillary flows is diminished. Let us emphasize that although the interfaces of the droplet and the substrate are motionless,

https://doi.org/10.1017/jfm.2022.814 Published online by Cambridge University Press

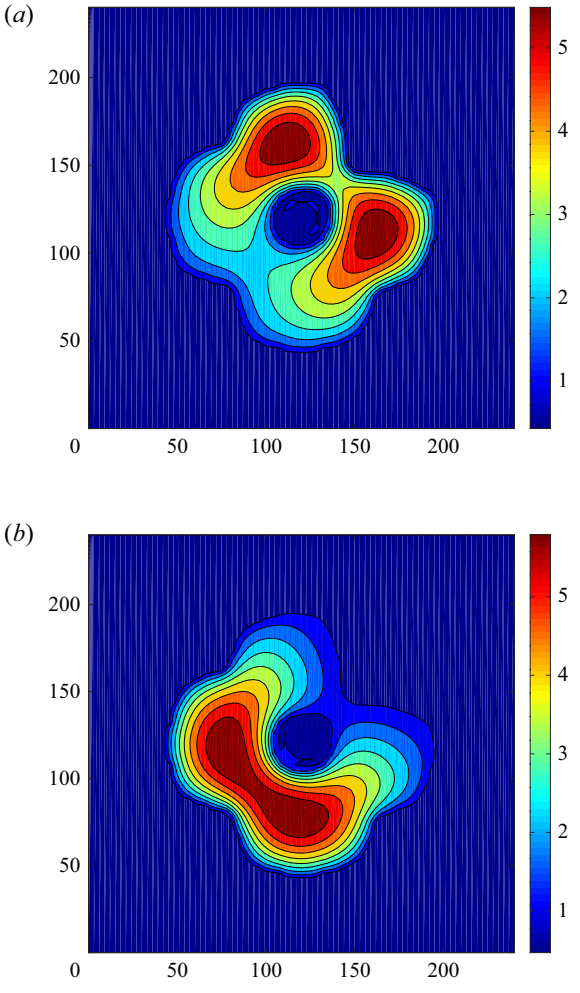


Figure 5. A snapshot of the fields of $h_2(X, Y, \tau)$ at (*a*) $\tau = 6.9 \times 10^5$ and (*b*) $\tau = 7 \times 10^5$ for $M = -4$, $Bo = 0$, $Bi = 20$.

there are thermocapillary flows in both the droplet and the substrate. The stresses created by those flows determine the shapes of the droplet surfaces, which are close to parabolic ones (see figure 2).

With an increase of cooling from below or heating from above, the droplet becomes oscillatory unstable.

The long-wave oscillatory instability of this type was formerly found in a system of two flat liquid layers (Nepomnyashchy & Simanovskii 2007). Because we consider here only the long-wave instability of a flat droplet, we expect that the physical origin of the droplet's instability is essentially the same as in the case of layers, i.e. it is caused by the interaction between deformations of both interfaces mediated by the thermocapillary flow, which is generated by those deformations. Qualitatively, by heating from above, Newton's law at the upper droplet surface creates a certain kind of negative feedback, which in the case of two interfaces can lead to an 'overstability', i.e. an oscillatory instability. Note that oscillatory Marangoni instabilities by heating from above have been observed also in some other problems (see Nepomnyashchy *et al.* 2012).

https://doi.org/10.1017/jfm.2022.814 Published online by Cambridge University Press

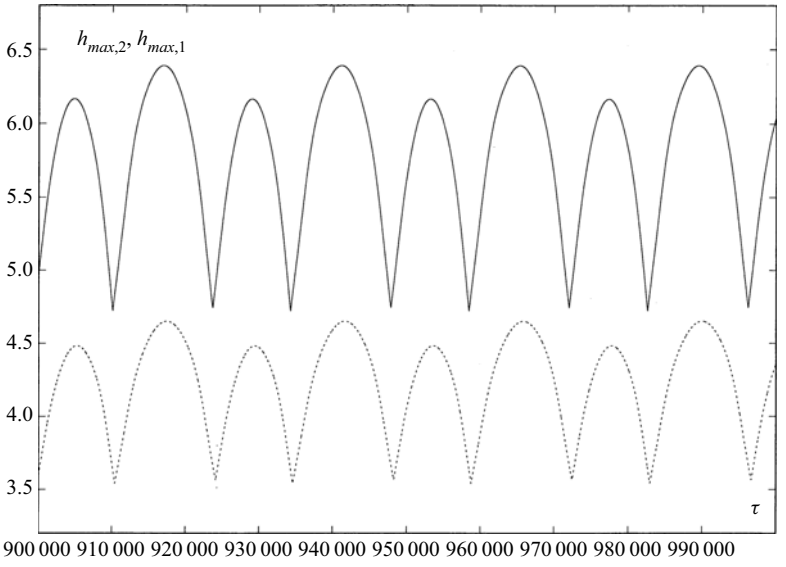


Figure 6. The oscillations of $h_{max,2}(\tau)$ (solid line) and $h_{max,1}(\tau)$ (dashed line) for $M = -4$, $Bo = 0$, $Bi = 20$.

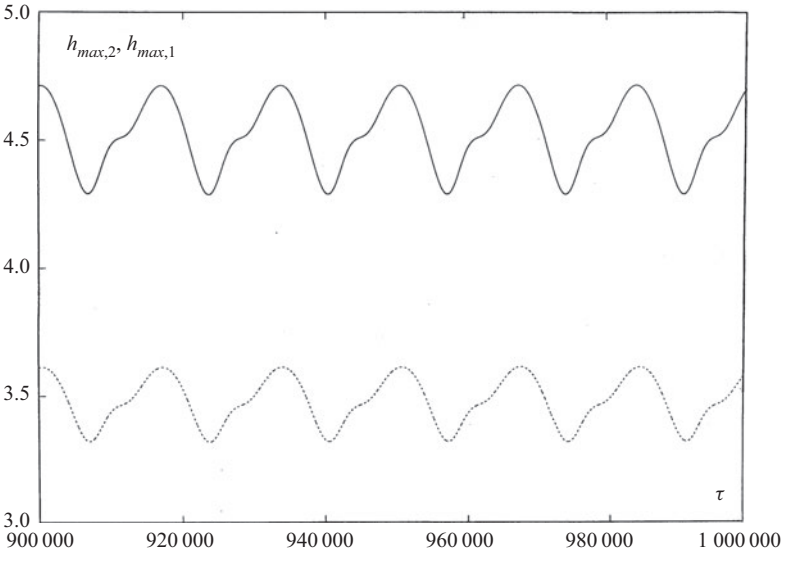


Figure 7. The oscillations of $h_{max,2}(\tau)$ (solid line) and $h_{max,1}(\tau)$ (dashed line) for $\bar{M} = -2.5$, $Bo = 0$, $Bi = 20$, $A = 0.25$, $\omega = 0.000375$.

At $M \leq -2.25$ we observe periodic oscillations characterized by the violation of the rotational symmetry, which corresponds to the azimuthal wavenumber $m = 1$ (see figure 3). The oscillations are characterized by the symmetry

$$h_m(X, Y, \tau + T/2) = h_m(L - Y, L - X, \tau), \quad m = 1, 2, \tag{3.4}$$

where T is the period of oscillations. In other words, after a half-period, the shape of the droplet is reflected with respect to the axis $X + Y = L$. Therefore, the quantities $h_{max,m}(\tau) = \max h_m(X, Y, \tau)$ and $h_{min,m}(\tau) = \min h_m(X, Y, \tau)$ are periodic in time with

https://doi.org/10.1017/jfm.2022.814 Published online by Cambridge University Press

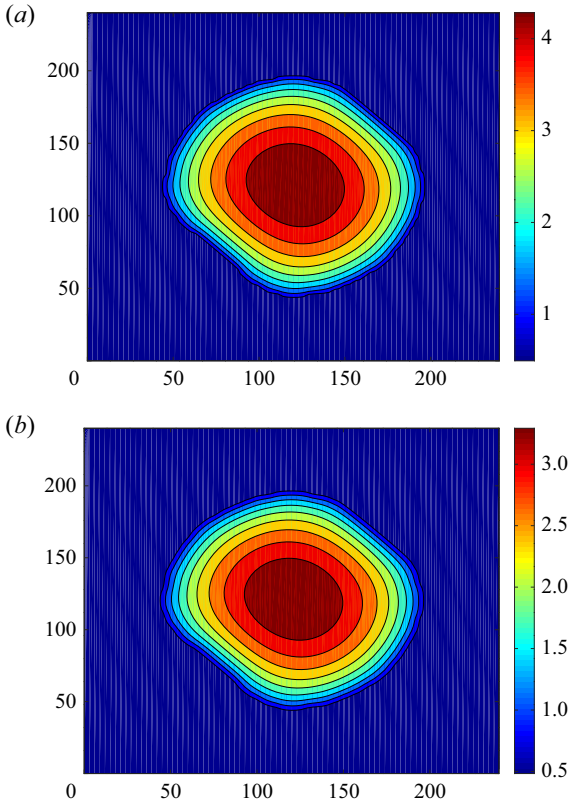


Figure 8. A snapshot of the fields of (*a*) $h_2(X, Y, \tau)$ and (*b*) $h_1(X, Y, \tau)$ for $\bar{M} = -2.5$, $Bo = 0$, $Bi = 20$, $A = 0.25$, $\omega = 0.000375$, $\tau = 1 \times 10^6$.

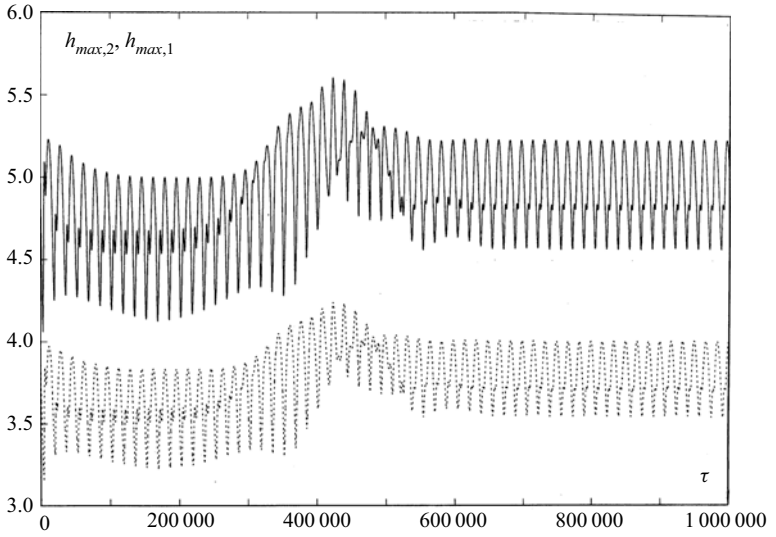


Figure 9. The oscillations of $h_{max,2}(\tau)$ (solid line) and $h_{max,1}(\tau)$ (dashed line) for $\bar{M} = -2.5$, $Bo = 0$, $Bi = 20$, $A = 0.5$, $\omega = 0.000375$; as initial conditions we use the structure shown in figure 10.

https://doi.org/10.1017/jfm.2022.814 Published online by Cambridge University Press

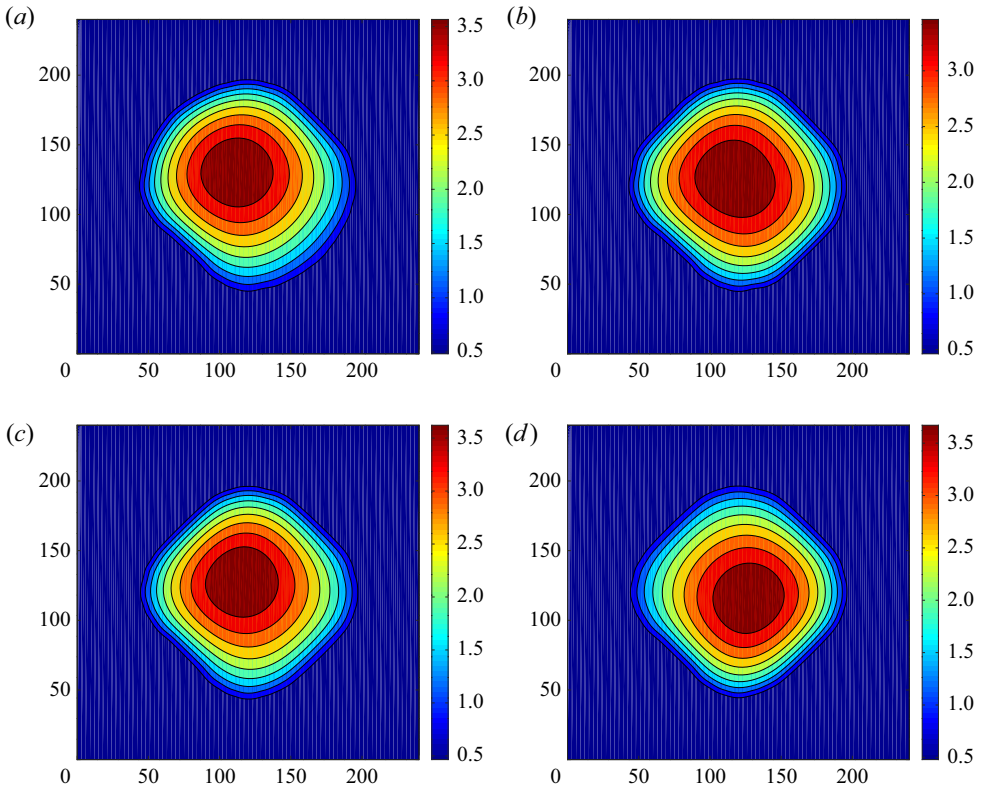


Figure 10. The fields of $h_2(X, Y, \tau)$ for $\bar{M} = -2.5$, $Bo = 0$, $Bi = 20$, $A = 0.5$, $\omega = 0.000375$: (*a*) $\tau = 100$; (*b*) $\tau = 1000$; (*c*) $\tau = 4000$; (*d*) $\tau = 10\,000$.

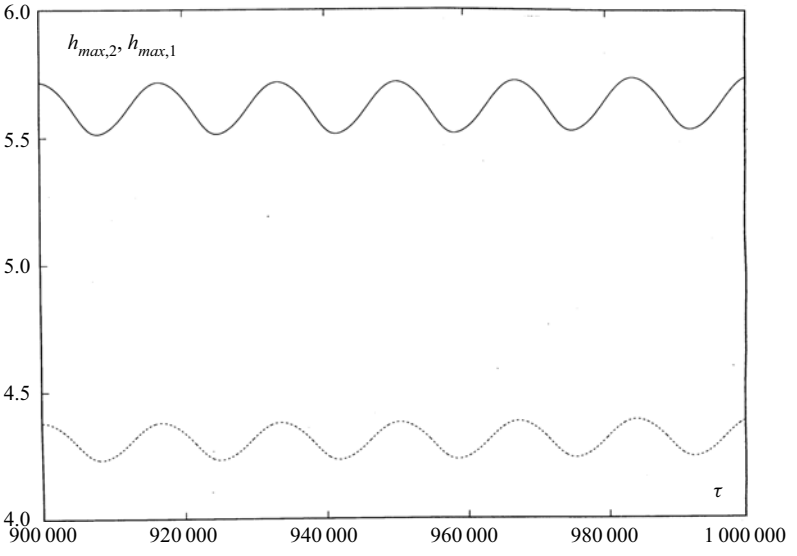


Figure 11. The oscillations of $h_{max,2}(\tau)$ (solid line) and $h_{max,1}(\tau)$ (dashed line) for $\bar{M} = -2.5$, $Bo = 0$, $Bi = 20$, $A = 0.25$, $\omega = 0.000375$.

https://doi.org/10.1017/jfm.2022.814 Published online by Cambridge University Press

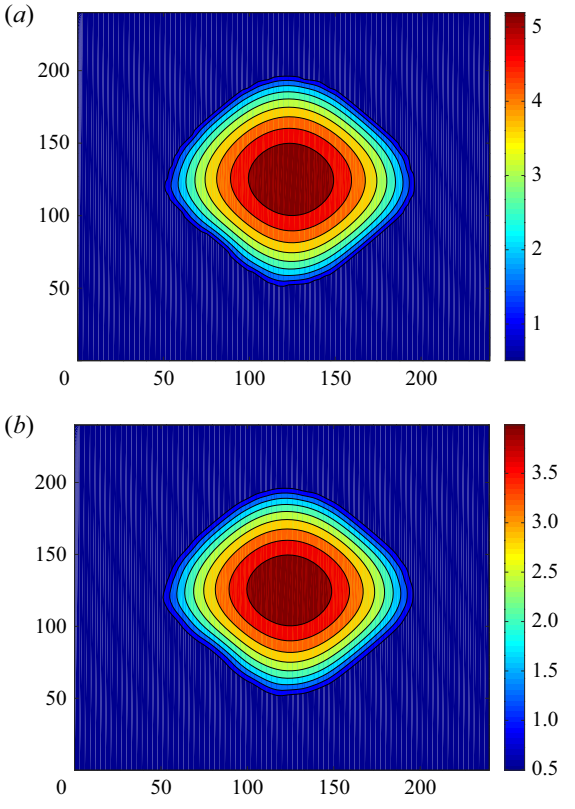


Figure 12. A snapshot of the fields of (*a*) $h_2(X, Y, \tau)$ and (*b*) $h_1(X, Y, \tau)$ for $\bar{M} = -2.5$, $Bo = 0$, $Bi = 20$, $A = 0.25$, $\omega = 0.000375$, $\tau = 1 \times 10^6$.

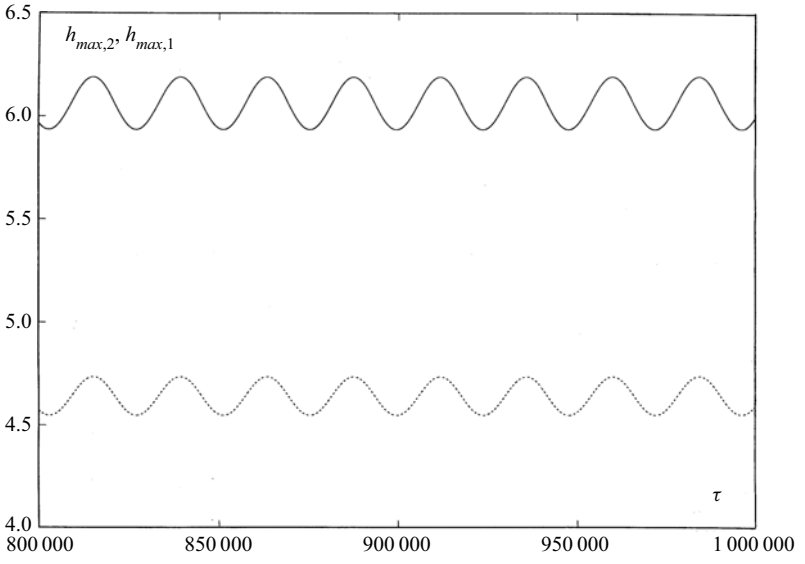


Figure 13. The oscillations of $h_{max,2}(\tau)$ (solid line) and $h_{max,1}(\tau)$ (dashed line) for $\bar{M} = -4$, $Bo = 0$, $Bi = 20$, $A = 0.25$, $\omega = 0.00026$.

https://doi.org/10.1017/jfm.2022.814 Published online by Cambridge University Press

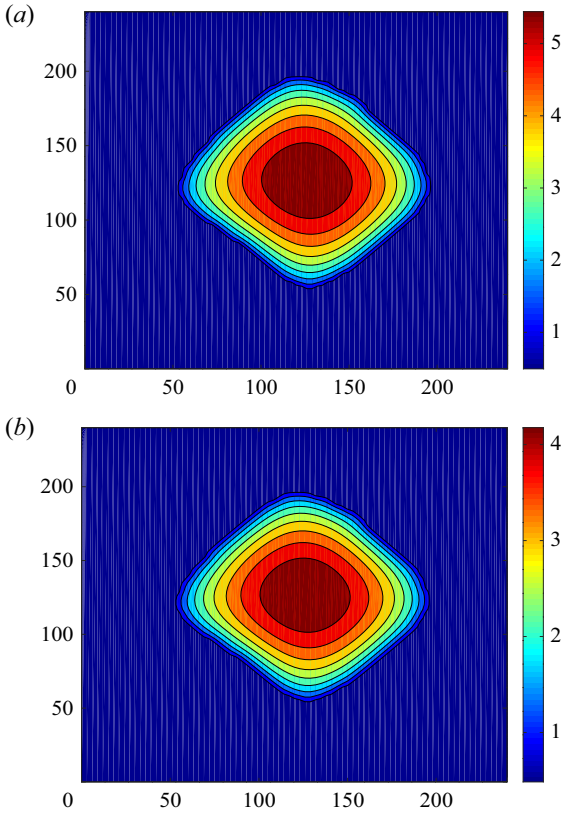


Figure 14. A snapshot of the fields of (*a*) $h_2(X, Y, \tau)$ and (*b*) $h_1(X, Y, \tau)$ for $\bar{M} = -4$, $Bo = 0$, $Bi = 20$, $A = 0.25$, $\omega = 0.00026$, $\tau = 1 \times 10^6$.

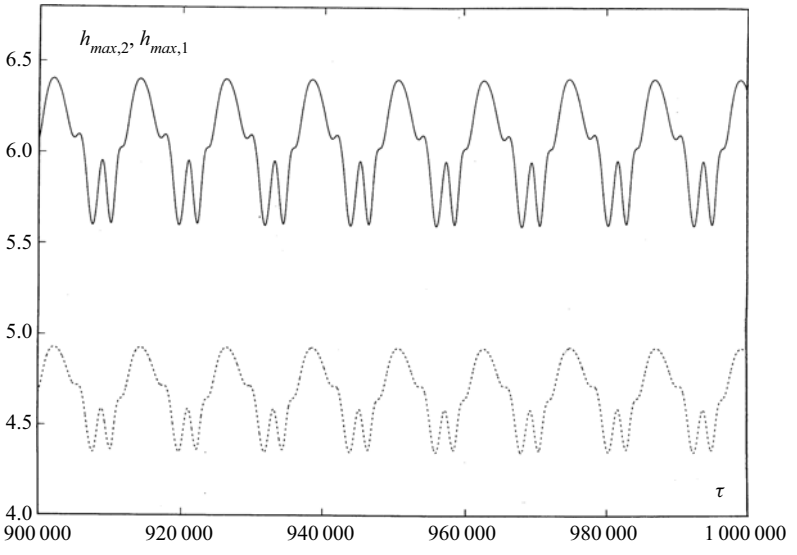


Figure 15. The oscillations of $h_{max,2}(\tau)$ (solid line) and $h_{max,1}(\tau)$ (dashed line) for $\bar{M} = -4$, $Bo = 0$, $Bi = 20$, $A = 0.75$, $\omega = 0.00052$.

https://doi.org/10.1017/jfm.2022.814 Published online by Cambridge University Press

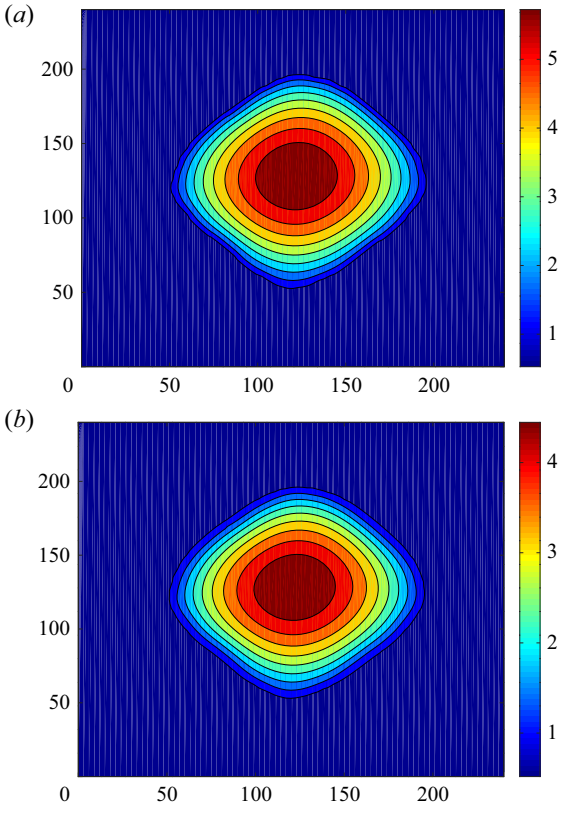


Figure 16. A snapshot of the fields of (*a*) $h_2(X, Y, \tau)$ and (*b*) $h_1(X, Y, \tau)$ for $\bar{M} = -4$, $Bo = 0$, $Bi = 20$, $A = 0.75$, $\omega = 0.00052$, $\tau = 1 \times 10^6$.

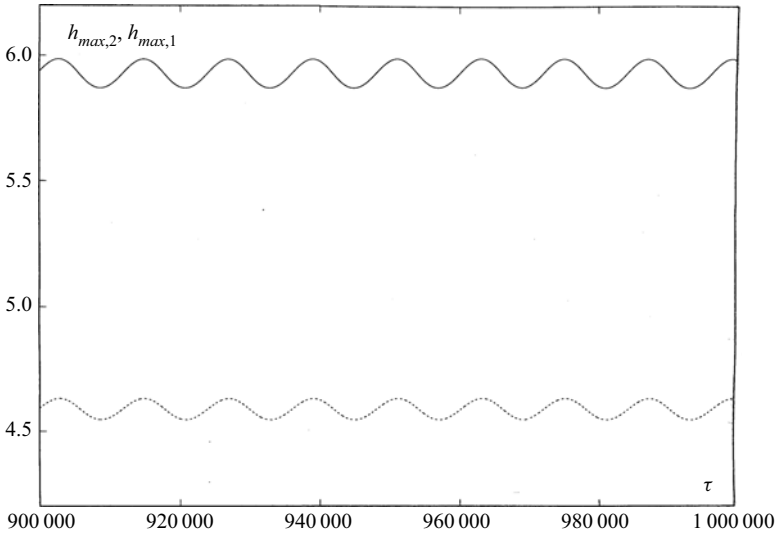


Figure 17. The oscillations of $h_{max,2}(\tau)$ (solid line) and $h_{max,1}(\tau)$ (dashed line) for $\bar{M} = -4$, $Bo = 0$, $Bi = 20$, $A = 0.1$, $\omega = 0.00052$.

https://doi.org/10.1017/jfm.2022.814 Published online by Cambridge University Press

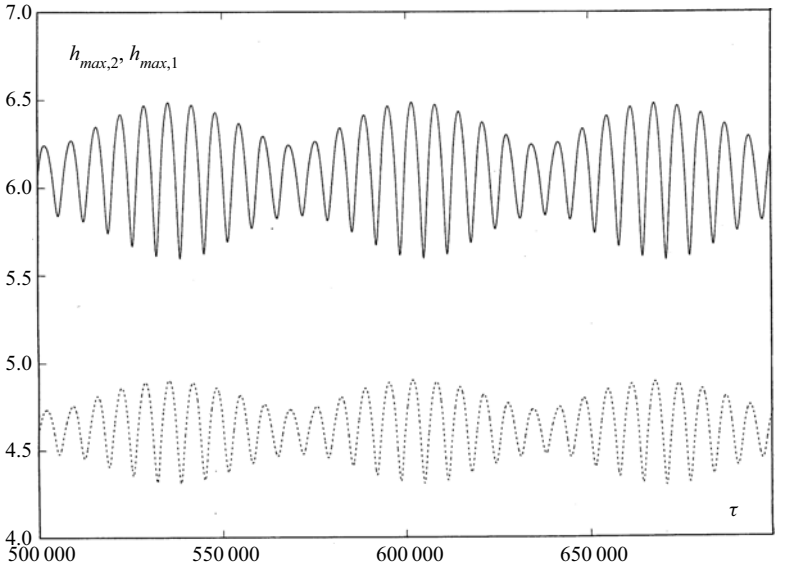


Figure 18. The oscillations of $h_{max,2}(\tau)$ (solid line) and $h_{max,1}(\tau)$ (dashed line) for $\bar{M} = -4$, $Bo = 0$, $Bi = 20$, $A = 0.1$, $\omega = 0.00104$.

period $T/2$. The temporal evolution of $h_{max,1}$ and $h_{max,2}$ is shown in figure 4. The type of oscillations described above is observed up to $|M| = 2.75$.

At higher values of $|M|$, the intensive Marangoni convection leads to a significant change of the droplet shape: a trough near the centre of the droplet is developed and the components with $m = 3$ and $m = 4$ become visible (see figure 5). Let us note that the structures presented in figure 5 have also been obtained on 100×100 and 120×120 grids. The spatial symmetry with respect to the axis $X = Y$ is retained, but the symmetry of oscillations (3.4) is violated; therefore the oscillation period of $h_{max,m}$ and $h_{min,m}$ becomes equal to the full period T. The temporal evolution of $h_{max,1}$ and $h_{max,2}$ is shown in figure 6.

3.3. *Time-periodic oscillations*

We apply time-periodic modulation of the Marangoni number M, determined by the formula

$$M(\tau) = \bar{M}(1 + A \sin \omega\tau), \quad \omega = 2\pi/T, \tag{3.5}$$

where A is the amplitude and ω is the frequency of modulation.

First, we explore the influence of heating modulation (3.5) on a stationary droplet of liquid 2 on a layer of liquid 1.

Let us take the round stationary droplet shown in figure 2 as initial condition and consider its evolution under the action of temporal modulation with $\bar{M} = -2.5$ and $\omega = 0.000375$. The oscillations of $h_{max,m}(\tau)$, $m = 1, 2$, of the initially round droplet are shown in figure 7 and a snapshot of the fields of $h_2(X, Y, \tau)$ and $h_1(X, Y, \tau)$ is presented in figure 8.

One can see that the shape of oscillations created by heating modulation with $\bar{M} = -2.5$ is quite different from those generated by the internal instability of the thermocapillary flow at $M = -2.5$ (compare figures 7 and 4; 8 and 3). The basic effect is a change of the droplet's shape.

https://doi.org/10.1017/jfm.2022.814 Published online by Cambridge University Press

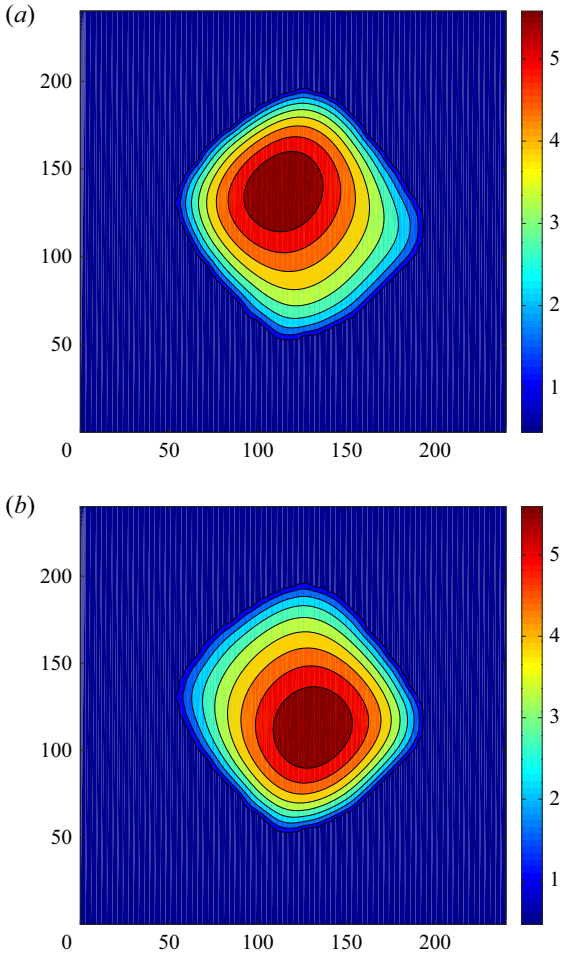


Figure 19. A snapshot of the fields of $h_2(X, Y, \tau)$ at (*a*) $\tau = 540\,000$ and (*b*) $\tau = 560\,000$ for $\bar{M} = -4$, $Bo = 0$, $Bi = 20$, $A = 0.1$, $\omega = 0.00104$.

If we use as initial conditions the periodic oscillations of the droplet shown in figure 8 and switch off modulation putting $A = 0$, we get a steady non-round droplet similar to those presented in figure 8. As found in Nepomnyashchy & Simanovskii (2021), the threshold of the appearance of spontaneous droplet oscillations depends on the shape of the droplet. For a round droplet, the threshold value of oscillatory instability is $|M_c| \approx 2.25 < 2.5$, while for the steady droplet, $|M_c| > 2.5$. That is why we observe periodic oscillations with the period of the external heating modulation, rather than a superposition of oscillations with two different frequencies, external and internal ones.

If we use initial conditions corresponding to figure 8 and increase the amplitude of modulation taking $A = 0.5$, we get a further change of the droplet's shape: the droplet becomes 'rhombic'. The transient process of the change of oscillations and the evolution of the droplet's shape are shown in figures 9 and 10.

With a decrease of the amplitude of modulation (we take $A = 0.25$), the periodic oscillations of the rhombic droplet become of a rather simple form (see figure 11). A snapshot of the fields of $h_2(X, Y, \tau)$ and $h_1(X, Y, \tau)$ is shown in figure 12. Thus, for the same values of parameters ($\bar{M} = -2.5$, $Bo = 0$, $Bi = 20$, $A = 0.25$ and $\omega = 0.000375$),

https://doi.org/10.1017/jfm.2022.814 Published online by Cambridge University Press

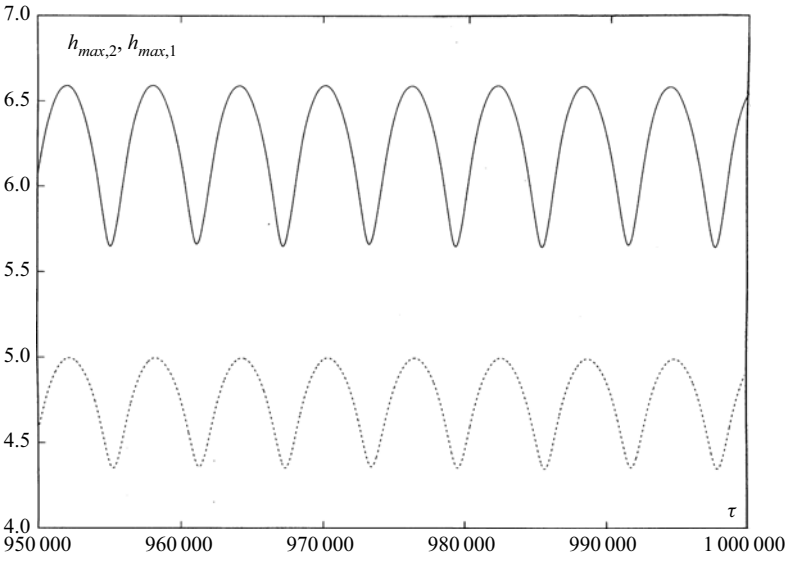


Figure 20. The oscillations of $h_{max,2}(\tau)$ (solid line) and $h_{max,1}(\tau)$ (dashed line) for $\bar{M} = -4$, $Bo = 0$, $Bi = 20$, $A = 0.25$, $\omega = 0.00104$.

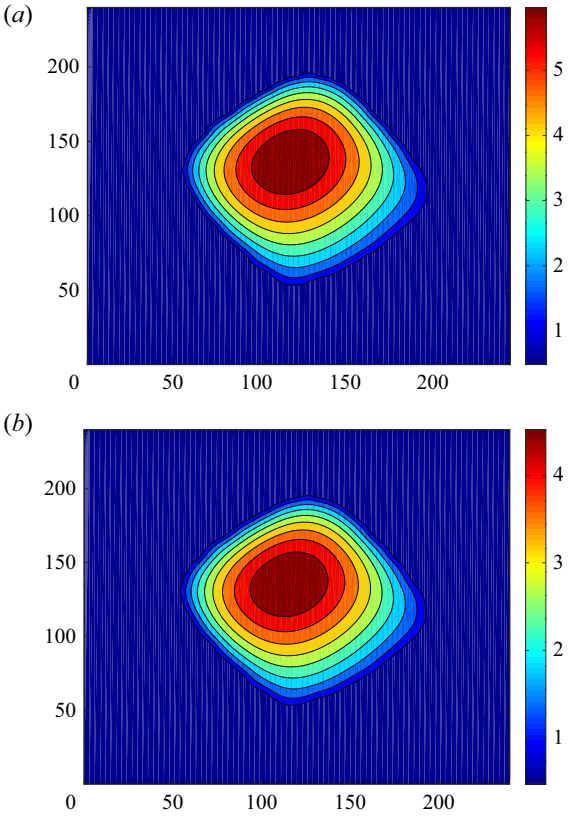


Figure 21. A snapshot of the fields of (*a*) $h_2(X, Y, \tau)$ and (*b*) $h_1(X, Y, \tau)$ for $\bar{M} = -4$, $Bo = 0$, $Bi = 20$, $A = 0.25$, $\omega = 0.00104$, $\tau = 1 \times 10^6$.

https://doi.org/10.1017/jfm.2022.814 Published online by Cambridge University Press

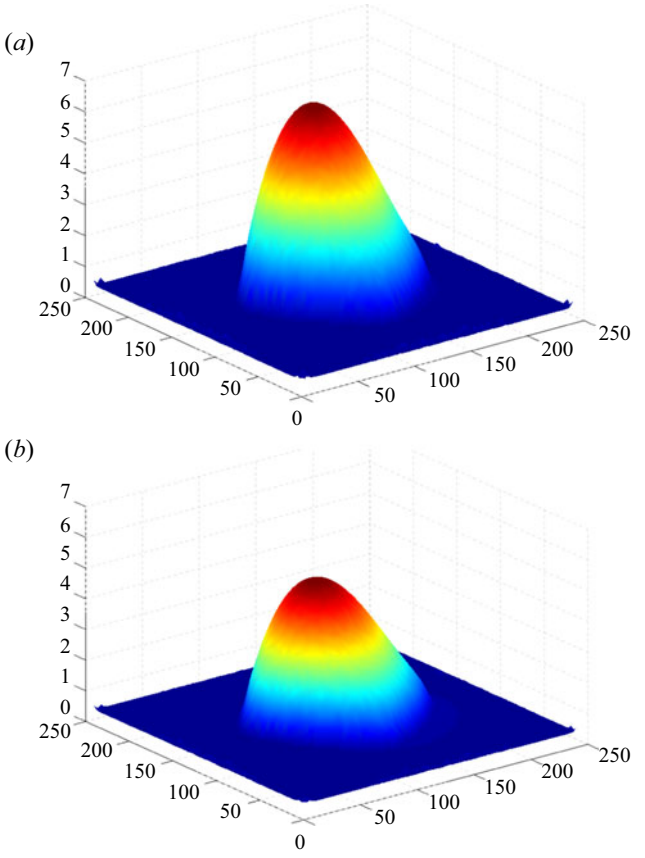


Figure 22. The shapes of (*a*) interface $h_2(X, Y, \tau)$ and (*b*) interface $h_1(X, Y, \tau)$ for $\bar{M} = -4$, $Bo = 0$, $Bi = 20$, $A = 0.25$, $\omega = 0.00104$, $\tau = 1 \times 10^6$.

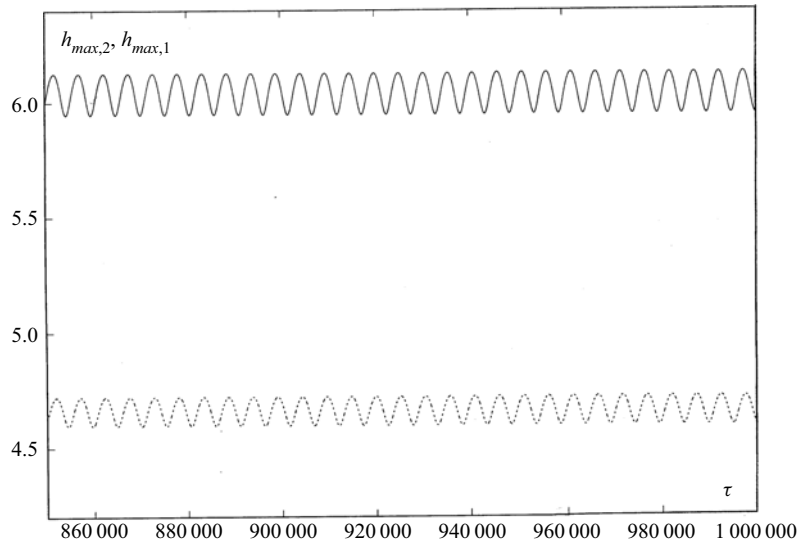


Figure 23. The oscillations of $h_{max,2}(\tau)$ (solid line) and $h_{max,1}(\tau)$ (dashed line) for $\bar{M} = -4$, $Bo = 0$, $Bi = 20$, $A = 0.1$, $\omega = 0.0012$.

https://doi.org/10.1017/jfm.2022.814 Published online by Cambridge University Press

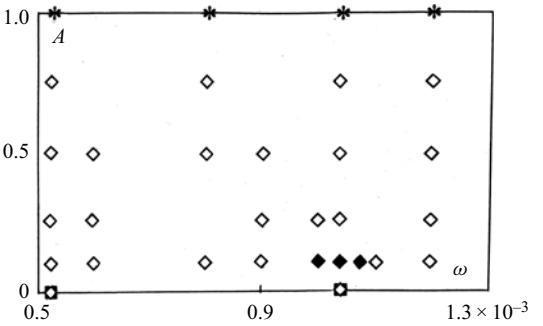


Figure 24. The diagram of flow regimes in the plane (ω, A) for $M = -4$, $Bo = 0$, $Bi = 20$. White diamonds, periodic oscillations; black diamonds, beatings; black squares, steady states; asterisks, irregular oscillations.

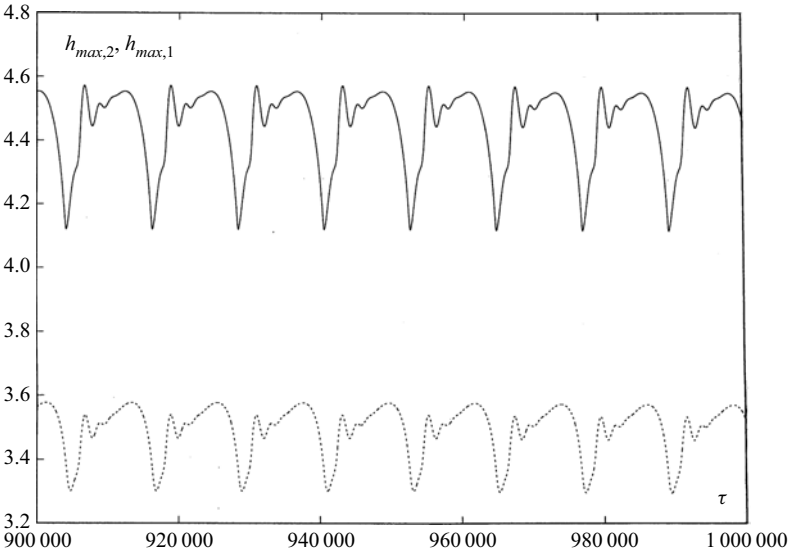


Figure 25. The oscillations of $h_{max,2}(\tau)$ (solid line) and $h_{max,1}(\tau)$ (dashed line) for $\bar{M} = -4$, $Bo = 0.05$, $Bi = 20$, $A = 0.75$, $\omega = 0.00052$.

we get droplets of different shape from different initial conditions. The characteristics of oscillations are strongly influenced by the droplet's shape. Indeed, the response of the system to an external perturbation depends on the set of eigenfrequencies and eigenfunctions of own droplet oscillations, which is determined by the droplet's shape.

If we use as initial conditions the periodic oscillations of the rhombic droplet (see figure 12) and switch off modulation, i.e. take $A = 0$, we get a steady rhombic droplet similar to those presented in figure 12. Therefore, there is no competition of frequencies. The rhombic droplet oscillates exactly with the imposed period of oscillations whatever it is. Note that in the case $M = -2.5$ and $A = 0$, we get tristability: (i) periodic oscillations of the round droplet obtained in the absence of modulation and two different shapes of a steady droplet, namely (ii) steady round droplet and (iii) steady rhombic droplet.

Now, let us increase cooling from below. For $M = -4$, the round droplet oscillates even without modulation – it has its own frequency (see figures 5 and 6). When we add modulation with another frequency, generally we can get oscillations with two

https://doi.org/10.1017/jfm.2022.814 Published online by Cambridge University Press

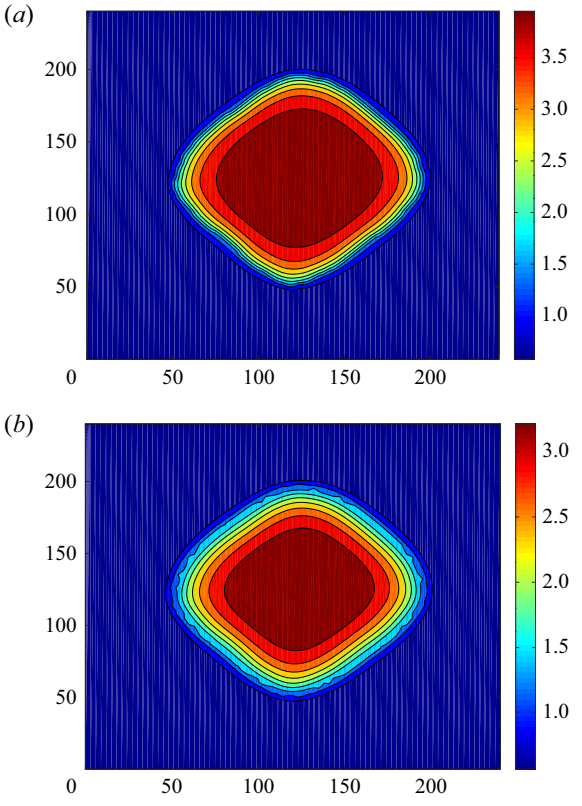


Figure 26. A snapshot of the fields of (*a*) $h_2(X, Y, \tau)$ and (*b*) $h_1(X, Y, \tau)$ for $\bar{M} = -4$, $Bo = 0.05$, $Bi = 20$, $A = 0.75$, $\omega = 0.00052$, $\tau = 1 \times 10^6$.

different frequencies. However, if we impose a heating modulation with the 'main frequency' $\omega = 0.00026$ close to the frequency of spontaneous oscillations, we observe periodic oscillations of a rhombic droplet shown in figure 13. A snapshot of the fields of $h_2(X, Y, \tau)$ and $h_1(X, Y, \tau)$ is presented in figure 14.

Periodic oscillations of the rhombic droplet with different amplitudes of modulation have been obtained also for the frequency $\omega_1 = 2\omega$. Oscillations of $h_{max,m}(\tau)$, $m = 1, 2$, for $A = 0.75$ are shown in figure 15 and a snapshot of the fields of $h_2(X, Y, \tau)$ and $h_1(X, Y, \tau)$ is presented in figure 16. With a decrease of the amplitude of modulation, oscillations of $h_{max,m}(\tau)$, $m = 1, 2$, are simplified (see figure 17).

3.4. *Non-periodic versus periodic oscillations*

Now, let us consider temporal modulation for $\bar{M} = -4$ with the frequency $\omega_2 = 4\omega$. In that case, we do not observe a synchronization of internal oscillations to the external modulation, and the motion is quasiperiodic. An example of the quasiperiodic oscillations of $h_2(X, Y, \tau)$ and $h_1(X, Y, \tau)$ is presented in figure 18. Snapshots of the fields of $h_2(X, Y, \tau)$ at different instants of time are shown in figure 19. Note that observed oscillations of the rhombic droplet take place along the other diagonal of the computational region than those shown in figure 5.

With an increase of the amplitude, the modulation frequency 'wins' and we get periodic oscillations of the rhombic droplet (see figure 20). A snapshot of the fields of $h_2(X, Y, \tau)$

https://doi.org/10.1017/jfm.2022.814 Published online by Cambridge University Press

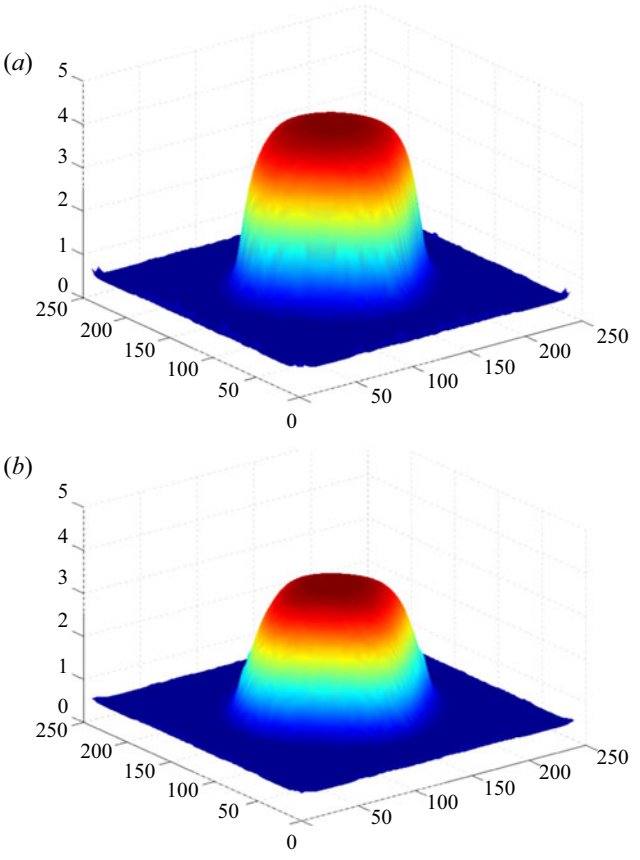


Figure 27. The shapes of (*a*) interface $h_2(X, Y, \tau)$ and (*b*) interface $h_1(X, Y, \tau)$ for $\bar{M} = -4$, $Bo = 0.05$, $Bi = 20$, $A = 0.75$, $\omega = 0.00052$, $\tau = 1 \times 10^6$.

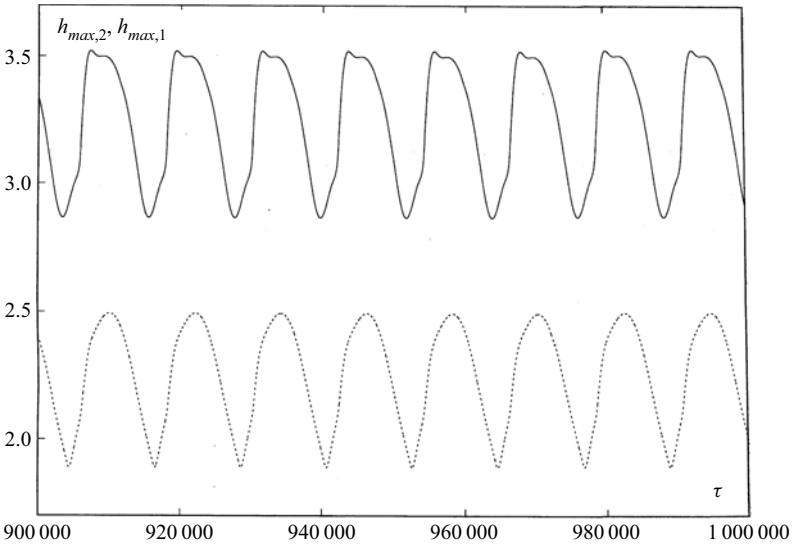


Figure 28. The oscillations of $h_{max,2}(\tau)$ (solid line) and $h_{max,1}(\tau)$ (dashed line) for $\bar{M} = -4$, $Bo = 0.2$, $Bi = 20$, $A = 0.75$, $\omega = 0.00052$.

https://doi.org/10.1017/jfm.2022.814 Published online by Cambridge University Press

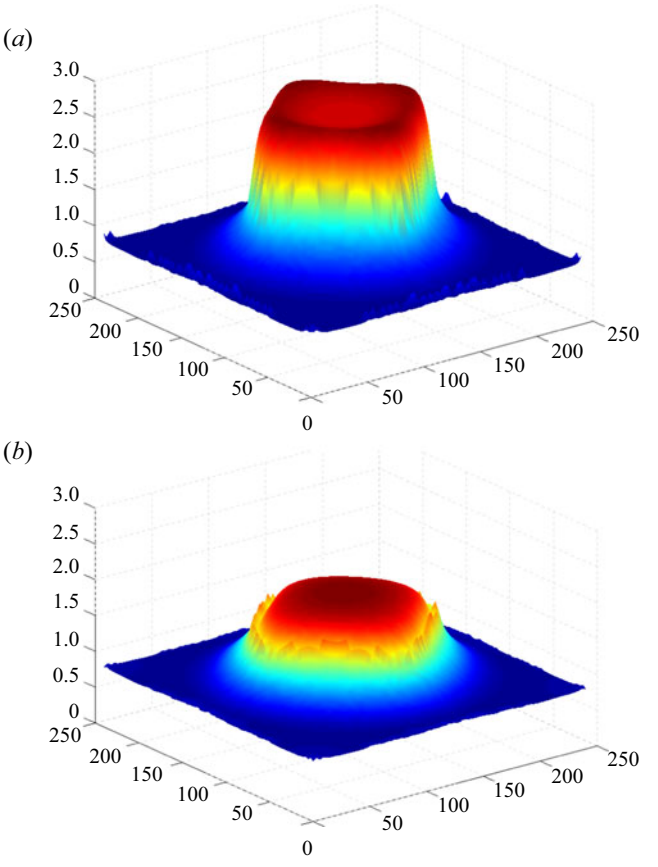


Figure 29. The shapes of (*a*) interface $h_2(X, Y, \tau)$ and (*b*) interface $h_1(X, Y, \tau)$ for $\bar{M} = -4$, $Bo = 0.2$, $Bi = 20$, $A = 0.75$, $\omega = 0.00052$, $\tau = 1 \times 10^6$.

and $h_1(X, Y, \tau)$ is shown in figure 21 and the shapes of interfaces are presented in figure 22. The periodic oscillations of the rhombic droplet on $\omega_2 = 4\omega$ have been also obtained for larger values of the amplitude of modulation ($A = 0.5$ and $A = 0.75$; see figure 24).

If we take as initial conditions the snapshot corresponding to quasiperiodic oscillations presented in figure 18 and increase the frequency (we take $\omega = 0.0012$), the modulation frequency wins and we get periodic oscillations of the rhombic droplet shown in figure 23. The diagram of regimes in the plane (ω, A) is constructed in figure 24.

3.5. *The influence of gravity on droplet dynamics*

Now, let us consider the action of gravity on the droplets. If we take the rhombic droplet shown in figure 16 as the initial condition (frequency $\omega_1 = 2\omega$), under the action of gravity ($Bo = 0.05$) the amplitude of periodic oscillations decreases (cf. figures 25 and 15) and the droplet is essentially flattened. A snapshot of the fields of $h_2(X, Y, \tau)$ and $h_1(X, Y, \tau)$ is shown in figure 26 and the shapes of interfaces are presented in figure 27.

With an increase of gravity (we take $Bo = 0.2$), the amplitude of periodic oscillations essentially decreases (cf. figures 28 and 25). The shapes of interfaces $h_2(X, Y, \tau)$ and $h_1(X, Y, \tau)$ are presented in figure 29. Let us emphasize that the dependence of the liquid–gas interface height on the distance from the droplet centre becomes

https://doi.org/10.1017/jfm.2022.814 Published online by Cambridge University Press

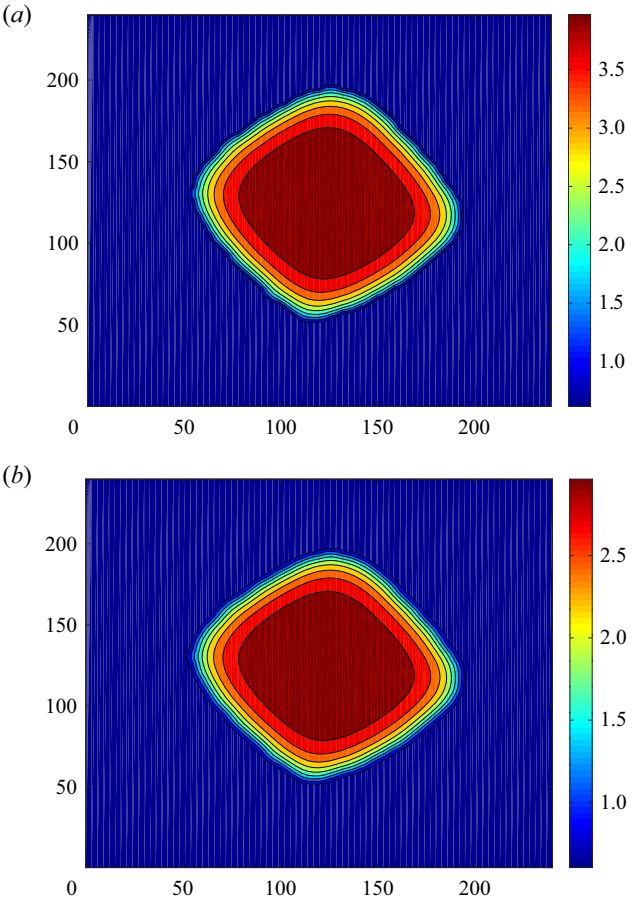


Figure 30. A snapshot of the fields of (*a*) $h_2(X, Y, \tau)$ and (*b*) $h_1(X, Y, \tau)$ for $\bar{M} = -4$, $Bo = 0.05$, $Bi = 20$, $A = 0.25$, $\omega = 0.00104$, $\tau = 1 \times 10^6$.

non-monotonic, so that this interface resembles an 'inkpot'. The upper boundary of the droplet oscillates in the vertical direction around a nearly flat position. During part of the period, it is bent down forming an inkpot, and during another part of the period it is bent up, and thus there is no inkpot. Let us note that it is quite natural when a flat surface of the droplet with a small stationary value of $\partial^2 h/\partial z^2$ at the droplet's top point starts to oscillate, then during a part of the time $\partial^2 h/\partial z^2 > 0$ in the top point (and we get an inkpot) and during the rest of the time $\partial^2 h/\partial z^2 < 0$ (and there is no inkpot). Thus, the basic effect of the temporal heating modulation is a change of the droplet's shape.

If we take the rhombic droplet shown in figures 21 and 22 as the initial condition (frequency $\omega_2 = 4\omega$), under the action of gravity ($Bo = 0.05$) the amplitude of periodic oscillations decreases and the droplet is essentially flattened. A snapshot of the fields of $h_2(X, Y, \tau)$ and $h_1(X, Y, \tau)$ is shown in figure 30 and the shapes of interfaces are presented in figure 31. For sufficiently large Bo ($Bo > 1.2$), a 'frozen' steady structure develops in the system.

https://doi.org/10.1017/jfm.2022.814 Published online by Cambridge University Press

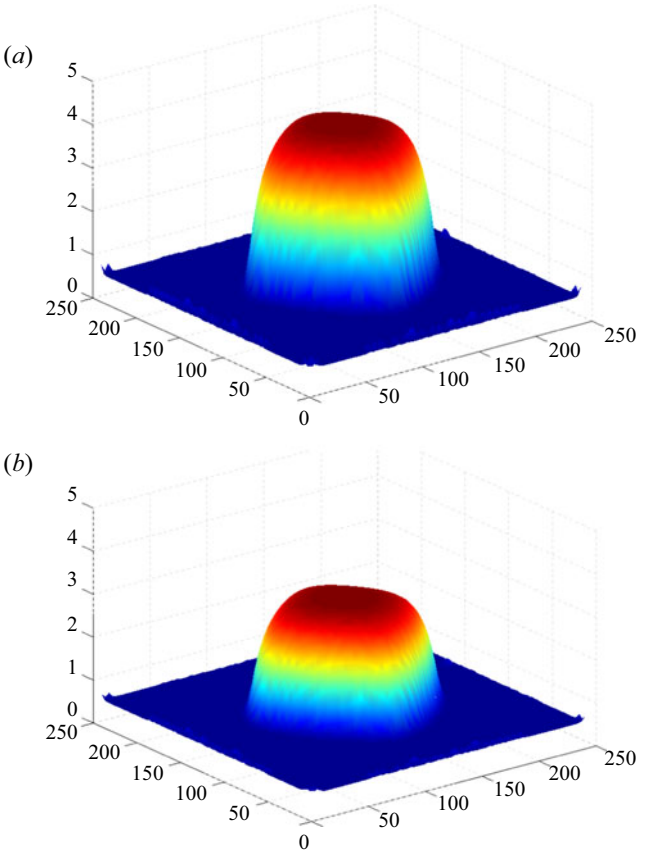


Figure 31. The shapes of (*a*) interface $h_2(X, Y, \tau)$ and (*b*) interface $h_1(X, Y, \tau)$ for $\bar{M} = -4$, $Bo = 0.05$, $Bi = 20$, $A = 0.25$, $\omega = 0.00104$, $\tau = 1 \times 10^6$.

4. Conclusions

The influence of the temporal modulation on Marangoni instabilities of droplets on a liquid substrate has been investigated. The problem has been studied numerically in the framework of long-wave amplitude equations and precursor model. It has been shown that temporal modulation can change the droplet's shape. Specifically, rhombic droplets have been obtained. The droplet's shape influences significantly the droplet's oscillations.

The effect of gravity has been taken into account. The gravity flattens the droplet and suppresses the oscillations, 'freezing' the droplet's shape.

In conclusion, let us estimate the physical values of parameters needed for the observation of the phenomena described in the paper. For the values of parameters $\eta_1 = 2.55 \times 10^{-2}\,\mathrm{kg\,m^{-1}\,s^{-1}}$, $H_1^0 = 5 \times 10^{-6}\,\mathrm{m}$, $\sigma_1^0 = 7.6 \times 10^{-3}\,\mathrm{N\,m^{-1}}$ and $L^* = 5 \times 10^{-5}\,\mathrm{m}$, applying the definition of the Marangoni number (2.3), we find that the value $M = -4$ used in our computations corresponds to a temperature difference $T_g - T_s = 0.5\,\mathrm{K}$.

Note that time scale (3.1*a*,*b*) is equal to $1.7 \times 10^{-1}\,\mathrm{s}$. Thus, the typical dimensional frequency of droplet oscillations observed in simulations is equal to 1.8×10^{-4}–$2.6 \times 10^{-4}\,\mathrm{s^{-1}}$.

Funding. This research was supported by the Israel Science Foundation (grant no. 843/18).

https://doi.org/10.1017/jfm.2022.814 Published online by Cambridge University Press

Declaration of interests. The authors report no conflict of interest.

Author ORCIDs.
Ilya Simanovskii https://orcid.org/0000-0002-4411-0522.

References

Buffone, C. 2019 Formation, stability and hydrothermal waves in evaporating liquid lenses. *Soft Matt.* **15**, 1970–1978.

Chen, Y.Z, Zhou, T.J., Li, Y.Y., Zhu, L.F., Handschuh-Wang, S., Zhu, D.Y., Zhou, X.H., Liu, Z., Gan, T.S. & Zhou, X.C. 2018 Robust fabrication of nonstick, noncorrosive, conductive graphene-coated liquid metal droplets for droplet-based, floating electrodes. *Adv. Funct. Mat.* **28**, 1706277.

Craster, R.V. & Matar, O.K. 2006 On the dynamics of liquid lenses. *J. Colloid Interface Sci.* **303**, 503–516.

Fisher, L.S. & Golovin, A.A. 2005 Nonlinear stability analysis of a two-layer thin liquid film: dewetting and autophobic behavior. *J. Colloid Interface Sci.* **291**, 515–528.

Géoris, P., Hennenberg, M., Lebon, G. & Legros, J.C. 1999 Investigation of thermocapillary convection in a three-liquid-layer systems. *J. Fluid Mech.* **389**, 209–228.

Gershuni, G.Z. & Lyubimov, D.V. 1998 *Thermal Vibrational Convection*. Wiley.

Gershuni, G.Z., Nepomnyashchy, A.A. & Velarde, M.G. 1992 On dynamic excitation of Marangoni instability. *Phys. Fluids* A **4**, 2394.

Huth, R., Jachalski, S., Kitavtsev, G. & Peschka, D. 2015 Gradient flow perspective on thin-film bilayer flows. *J. Engng Maths* **94**, 43–61.

Ju, G., Yang, X., Li, L., Cheng, M. & Shi, F. 2019 Removal of oil spills through a self-propelled smart device. *Chem.-Asian J.* **14**, 2435–2439.

Kriegsmann, J.J. & Miksis, M.J. 2003 Steady motion of a drop along a liquid interface. *SIAM J. Appl. Maths* **64**, 18–40.

Labanieh, L., Nguyen, T.N., Zhao, W.A. & Kang, D.K. 2015 Floating droplet array: an ultrahigh-throughput device for droplet trapping, real time analysis and recovery. *Micromachines* **60**, 1469–1482.

Manga, M. & Stone, H.A. 1995 Low Reynolds number motion of bubbles, drops and rigid spheres through fluid-fluid interfaces. *J. Fluid Mech.* **287**, 279–298.

Nepomnyashchy, A. & Simanovskii, I. 2010 Effect of gravity on the dynamics of non-isothermic ultra-thin two-layer films. *J. Fluid Mech.* **661**, 1–31.

Nepomnyashchy, A. & Simanovskii, I. 2012 Nonlinear Marangoni waves in a two-layer film in the presence of gravity. *Phys. Fluids* **24**, 032101.

Nepomnyashchy, A. & Simanovskii, I. 2020 Synchronization of Marangoni waves by temporal modulation of interfacial heat consumption. *Phys. Rev. Fluids* **5**, 094007.

Nepomnyashchy, A. & Simanovskii, I. 2021 Droplets on the liquid substrate: thermocapillary oscillatory instability. *Phys. Rev. Fluids* **6**, 034001.

Nepomnyashchy, A., Simanovskii, I. & Legros, J.C. 2012 *Interfacial Convection in Multilayer Systems*, 2nd edn. Springer.

Nepomnyashchy, A.A. & Simanovskii, I.B. 2007 Marangoni instability in ultrathin two-layer films. *Phys. Fluids* **19**, 122103.

Nepomnyashchy, A.A. & Simanovskii, I.B. 2015 Generation of nonlinear Marangoni waves in a two-layer film by heating modulation. *J. Fluid Mech.* **771**, 159–192.

Or, A.C. & Kelly, R.E. 2002 The effects of thermal modulation upon the onset of Marangoni-Bénard convection. *J. Fluid Mech.* **456**, 161–182.

Oron, A., Davis, S.H. & Bankoff, S.G. 1997 Long-scale evolution of thin liquid films. *Rev. Mod. Phys.* **69**, 931.

Pearson, J.R.A. 1958 On convection cells induced by surface tension. *J. Fluid Mech.* **4**, 489–500.

Pototsky, A., Bestehorn, M., Merkt, D. & Thiele, U. 2005 Morphology changes in the evolution of liquid two-layer films. *J. Chem. Phys.* **122**, 224711.

Pototsky, A., Oron, A. & Bestehorn, M. 2019 Vibration-induced flotation of a heavy liquid drop on a lighter liquid film. *Phys. Fluids* **31**, 087101.

Princen, H.M. 1969 Shape of interfaces, drops, and bubbles. In *Surface and Colloid Science*, 1st edn (ed. E. Matijevic), vol. 2. Wiley.

Rybalko, S., Magome, N. & Yoshikawa, K. 2004 Forward and backward laser-guided motion of an oil droplet. *Phys. Rev.* E **70**, 046301.

https://doi.org/10.1017/jfm.2022.814 Published online by Cambridge University Press

SCARDOVELLI, R. & ZALESKI, S. 1999 Direct numerical simulation of free surface and interfacial flow. *Annu. Rev. Fluid Mech.* **31**, 567–603.

SHIMAZAKI, Y., SHIRATORI, A., HARADA, K., NAKAGAWA, T., TANAKA, J. & UEMATSU, C. 2021 Dense array of floating water droplets aligned to an assembly of tubular wells. *Japan J. Appl. Phys.* **60**, 037002.

SMITH, K.A. 1966 On convection instability induced by surface tension gradient. *J. Fluid Mech.* **24**, 401–414.

SMITH, K.A., OTTINO, J.M. & DE LA CRUZ, M.O. 2004 Dynamics of a drop at a fluid interface under shear. *Phys. Rev.* E **69**, 046302.

SMORODIN, B.L., MIKISHEV, A.B., NEPOMNYASHCHY, A.A. & MYZNIKOVA, B.I. 2009 Thermocapillary instability of a liquid layer under heat flux modulation. *Phys. Fluids* **21**, 062102.

SONG, C., MOON, J.K., LEE, K., KIM, K. & PAK, H.K. 2014 Breathing, crawling, budding, and splitting of a liquid droplet under laser heating. *Soft Matt.* **10**, 2679–2684.

STERNLING, C.V. & SCRIVEN, L.E. 1964 On cellular convection driven by surface tension gradients: effects of mean surface tension and surface viscosity. *J. Fluid Mech.* **19**, 321–340.

YAMINI, Y., REZAZADEH, M. & SEIDI, S. 2019 Liquid-phase microextraction - the different principles and configurations. *TRAC-Trend. Anal. Chem.* **112**, 264–272.

https://doi.org/10.1017/jfm.2022.814 Published online by Cambridge University Press